

Near- and mid-infrared intersubband absorption in top-down GaN/AlN nano- and micropillars

Jonas Lähnemann,^{1,2,*} David A. Browne,¹ Akhil Ajay,¹ Jean-Luc Thomassin,¹ Edith Bellet-Amalric,¹ and Eva Monroy¹

¹*Université Grenoble-Alpes, CEA, INAC, PHELIQS, 17 av. des Martyrs, 38000 Grenoble, France*

²*Paul-Drude-Institut für Festkörperelektronik, Hausvogteiplatz 5–7, 10117 Berlin, Germany*

We present a systematic study of top-down processed GaN/AlN heterostructures for intersubband optoelectronic applications. Samples containing quantum well superlattices that display either near- or mid-infrared intersubband absorption were etched into nano- and micropillar arrays in an inductively coupled plasma. We investigate the influence of this process on the structure and strain-state, on the interband emission and on the intersubband absorption. Notably, for pillar spacings significantly smaller ($\leq 1/3$) than the intersubband wavelength, the magnitude of the intersubband absorption is not reduced even when 90% of the material is etched away and a similar linewidth is obtained. The same holds for the interband emission. Whereas for pillar spacings on the order of the intersubband absorption wavelength, photonic crystal resonances are observed. The presented results are a first step towards micro- and nanostructured group-III nitride devices relying on intersubband transitions.

I. INTRODUCTION

Engineering intersubband transitions between confined states in the conduction band of group-III arsenide quantum wells has led to the fabrication of both detectors and emitters across the mid- and far-infrared (IR) spectral ranges. In recent years, group-III nitride semiconductors have evolved into a promising alternative for the realization of intersubband technologies [1]. Advantages of the group-III nitrides can be found in their large conduction band offset, e.g. 1.8 eV for GaN/AlN [2–4], which offers the possibility to extend the operating range of intersubband devices into the near-IR spectral range, including the 1.3–1.55 μm wavelength window. Devices for fiber-optic telecommunications could also profit from the sub-picosecond intersubband relaxation times [5, 6]. Furthermore, the large longitudinal-optical (LO) phonon energy (91 meV) in GaN opens prospects for room-temperature operation of devices designed for THz frequencies [1, 7, 8].

Besides planar quantum well structures, a variety of three-dimensional geometries have been proposed in the past years. In particular, nanowires and micropillars are explored as a way to independently control the electrical and the optical device cross section by changing the diameter-to-pitch ratio in the array. Furthermore, the three-dimensional carrier confinement in nanowire heterostructures opens new possibilities to tune the carrier relaxation time. Such structures can be achieved by bottom-up growth or top-down etching. On the one hand, near-IR intersubband absorption could be demonstrated for GaN/AlN superlattices grown on self-assembled GaN nanowires [9]. In such nanowires, dispersed and processed into miniaturized photodetectors, an intersubband photocurrent was detected under near-IR illumination [10]. Despite the large lattice-mismatch between GaN and AlN, bottom-up nanowire heterostructures have low dislocation densities thanks to the elastic strain relaxation at the nanowire surface. However, this advantage comes at the expense of a wire-to-wire inhomogeneity of the superlattice

dimensions inherent to the self-assembled growth [11, 12]. As a consequence, the intersubband absorption is spectrally broad when compared to planar quantum wells [13] or quantum dots [14]. On the other hand, nano- and micropillar arrays for THz emission have been achieved by lithographically defined top-down etching of (Al,Ga)As heterostructures [15–17]. Particularly, Amanti *et al.* [15] have shown THz quantum-cascade lasing in a micropillar array, which due to its sub-wavelength dimensions could be considered as photonic metamaterial. In the case of photodetectors, by optimizing the pillar dimensions and spacing based on electrodynamics simulations of the light incoupling at the absorbed wavelength, pillar detectors can be expected to outperform planar detectors, while at the same time lifting selection rules concerning the polarization of the incoming light [18].

The aim of the current study is to investigate the influence of the top-down etching of nano- and micropillar arrays on the intersubband absorption in GaN/AlN heterostructures, to assess the suitability of this geometry for group-III nitride intersubband devices. To this end, we grew two samples designed to present intersubband transitions in the near- and mid-IR spectral ranges, respectively, and these were processed into micro-/nanopillars. Here, we show that when the spacing of the pillar array is comparable to the wavelength of the investigated spectral region, photonic crystal resonances dominate the IR absorption spectra. For sub-wavelength spacing, the intersubband absorption is recovered with similar linewidth as in the as-grown material. Furthermore, our work demonstrates that both the interband emission and the intersubband absorption signals are not attenuated according to the reduction of material during the top-down processing.

II. EXPERIMENTS AND METHODS

The investigated samples consist of superlattices of highly doped GaN/AlN quantum wells (QWs) grown by plasma-assisted molecular-beam epitaxy (PAMBE) on a 1 μm thick AlN-on-sapphire template. The growth conditions were described elsewhere [13]. Prior to the growth of the super-

* Electronic mail: laehnemann@pdi-berlin.de

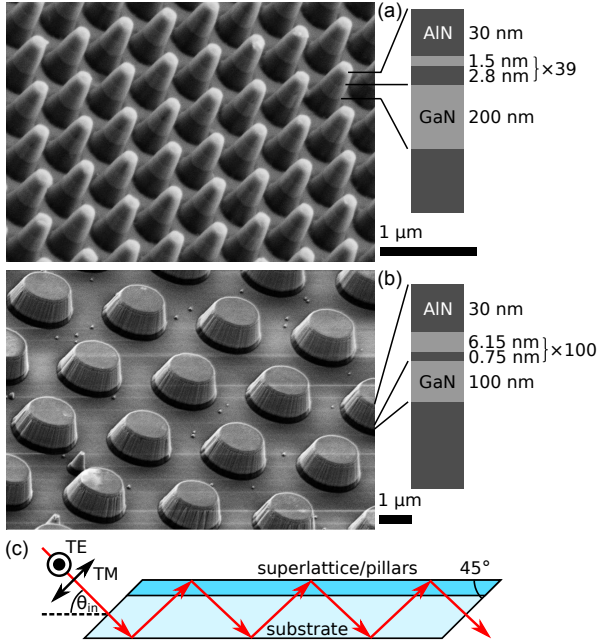


FIG. 1. Bird's-eye view SEM images and sketches of the layer stacks for samples (a) NIR etched into pillars with $d = 0.2 \mu\text{m}$ and (b) MIR with $d = 1.5 \mu\text{m}$. (c) Sketch of the waveguide geometry used for the FTIR measurements, indicating the incident angle of the light on the input facet θ_{in} and the criterion to define TE and TM polarization.

lattice, a 200 nm thick undoped GaN layer was deposited under Ga-rich conditions. This GaN buffer remains partially strained on AlN [19], which allows the growth of the superlattice without cracking. After the growth of the superlattice, a 30 nm thick AlN cap layer was deposited to prevent the depletion of the QWs due to surface states. The study was performed on two samples. The first of them (sample NIR) consists of 39 periods of 1.5 nm thick GaN:Si QWs separated by 2.8 nm thick AlN barriers. The second sample (sample MIR) consists of 100 periods of 6.15 nm thick GaN:Si QWs separated by 0.75 nm thick AlN barriers. Silicon was incorporated in the GaN QWs to reach a surface doping density of $1.6 \times 10^{13} \text{ cm}^{-2}$. The electronic levels in the QWs were calculated using the $\mathbf{k}\cdot\mathbf{p}$ module of the self-consistent Schrödinger-Poisson solver Nextnano [20] with the material parameters described in Ref. 13. The difference in energy between ground and first excited state of the electron in the QWs ($e_2 - e_1$), including corrections for many-body effects [4, 9], was calculated to be 0.81 eV ($\lambda \approx 1.53 \mu\text{m}$) for sample NIR and 0.29 eV ($\lambda \approx 4.33 \mu\text{m}$) for sample MIR, respectively.

Micro- and nanopillars were etched using a top-down process. To this end, a Ti/Ni (5/50 nm) etch mask of circular structures on a hexagonal grid was defined by lift-off. The pattern was written by laser lithography for pillars with a diameter $d = 1.5 \mu\text{m}$ (both samples) and electron beam lithography for diameters $d = 0.4, 0.2$ and $0.1 \mu\text{m}$ (only sample NIR). The pillar dimensions and pitch (center-to-center distance) are summarized in Table I. The material around

the pillars was removed with an inductively-coupled plasma (ICP) etch. The following parameters, optimized for steep sidewalls [21], were used: 10 sccm Cl_2 and 25 sccm Ar with an ICP power of 300 W and a radio-frequency power of 150 W at room temperature at a pressure of 5 mTorr. A 3 min etch leads to an etch depth of approximately 1100 nm. Subsequently, the metal mask was removed with FeCl_3 and HF. Exemplary scanning electron microscopy (SEM) images of the resulting nano- and micropillars are shown in Fig. 1(a) for sample NIR with $d = 0.2 \mu\text{m}$ and in Fig. 1(b) for sample MIR with $d = 1.5 \mu\text{m}$ together with sketches of the respective superlattice structures.

High-resolution x-ray diffraction (XRD) of the as-grown and processed samples was performed using a Rigaku SmartLab X-Ray diffractometer system with a 2-bounce Ge(220) monochromator and a 0.228° long plate collimator in front of the detector. The influence of etching on the interband emission was investigated by photoluminescence (PL) spectroscopy under excitation with a continuous-wave solid-state laser (wavelength $\lambda = 244 \text{ nm}$, laser power of $0.4 \mu\text{W}$) focused to a spot with a diameter of $\approx 100 \mu\text{m}$. The sample emission is passed through a grating monochromator and is detected using an ultraviolet-enhanced charge-coupled device. PL measurements were carried out at 300 and 10 K. The intersubband absorption was measured at room temperature in a Bruker 70v Fourier transform infrared (FTIR) spectrometer. For this purpose, the samples were polished into a waveguide geometry as sketched in Fig. 1(c). Thereby, the sample can be rotated to change the incident angle. The spectrometer is equipped with a halogen lamp (near-IR), an Hg discharge lamp (mid-IR), a CaF_2 beam splitter, and a nitrogen-cooled mercury-cadmium-telluride detector. The transverse electric (TE) and transverse magnetic (TM) polarization components were distinguished by polarizing the incident light with a linear polarizer placed in front of the sample. As the selection rules restrict the intersubband absorption to TM polarized light, the TM transmittance spectra were divided through the transmittance in TE polarization to correct for the system response.

III. RESULTS

A. Structure and strain-state

The structural characteristics of the GaN/AlN superlattice and the influence thereon of the top-down processing were investigated by high-resolution XRD. Figure 2(a) shows exemplary $\omega - 2\theta$ profiles around the (0002) reflection for sample NIR as-grown and etched into nanopillar arrays. Theoretical calculations using the Rigaku SmartLab Studio software are superimposed upon the experimental data. The superlattice period extracted from these $\omega - 2\theta$ scans is summarized in Table I for all investigated samples, together with the full width at half maximum (FWHM) of the ω -scan around the (0002) reflection of the superlattice ($\Delta\omega_{\text{SL}}$), the AlN template ($\Delta\omega_{\text{AlN}}$), and the GaN buffer layer ($\Delta\omega_{\text{GaN}}$). Variations in the superlattice period are due to a gradient

TABLE I : Summary of the sample characteristics, including pillar diameters and pitches. Structural parameters determined from XRD measurements include the superlattice (SL) period, the FWHM ($\Delta\omega$) of the ω -scans across the (0002) reflections of the SL, the AlN substrate and the GaN buffer, as well as the GaN c lattice constant in the buffer layer and the strain in the buffer layer ϵ_{zz} . From the PL measurements, the low-temperature integrated intensity $I_{PL}(10\text{ K})$ normalized to its value for the as-grown sample, as well as the ratio of room- and low- temperature intensities $I_{PL}(300\text{ K})/I_{PL}(10\text{ K})$ are given. Regarding the FTIR measurements, the center λ and FWHM of the absorption band, measured before and after etching, are given for the different samples.

Sample	NIR					MIR	
Diameter (μm)		1.5	0.4	0.2	0.1		1.5
Pitch (μm)	as-grown	3.0	1.2	0.6	0.3	as-grown	3.0
SL period ($\pm 0.1\text{ nm}$)	4.3	4.0	4.2	4.2	4.4	7.1	6.9
$\Delta\omega_{SL}$ ($^\circ$)	0.18	0.38	0.44	0.28	0.44	0.21	0.27
$\Delta\omega_{AlN}$ ($^\circ$)	0.06	0.06	0.06	0.05	0.05	0.06	0.07
$\Delta\omega_{GaN}$ ($^\circ$)	0.16	0.42	0.33	0.30	0.43	0.33	0.36
c_{GaN} ($\pm 0.002\text{ \AA}$)	5.208	5.192	5.185	5.183	5.186	5.211	5.198
ϵ_{zz} ($\pm 4 \times 10^{-4}$)	4.6×10^{-3}	1.5×10^{-3}	3×10^{-4}	-3×10^{-4}	4×10^{-4}	5.2×10^{-3}	2.7×10^{-3}
$I_{PL}(10\text{ K})$ (normalized)	1.0	0.68	0.73	0.96	0.65	1	0.75
$I_{PL}(300\text{ K})/I_{PL}(10\text{ K})$	0.10	0.08	0.07	0.03	0.05	–	–
λ_{FTIR} (as grown) (μm)	–	–	1.43	1.54	1.51	–	4.4
λ_{FTIR} (etched) (μm)	–	–	1.38	1.42	1.47	–	4.6
FWHM _{FTIR} (as grown) (μm)	–	–	0.28	0.33	0.32	–	1.4
FWHM _{FTIR} (etched) (μm)	–	–	0.28	0.31	0.4	–	1.8

of the growth rate along the wafer resulting from the radial variation of the active nitrogen flux impinging on the substrate. In the diffractogram of the as-grown material, the angular location of the reflection from the GaN buffer layer confirms that it remains partially strained by the AlN substrate. To be precise, the as-grown out-of-plane deformation is $\epsilon_{zz} = (c - c_0)/c_0 = (4.6 \pm 0.4) \times 10^{-3}$, with c being the measured out-of-plane lattice constant and $c_0 = 5.1850\text{ \AA}$ being the lattice constant for relaxed GaN. This value corresponds to a relaxation of GaN on AlN by only 65%, with the relaxation defined as $R(\%) = 100 \times (c_{FS} - c)/(c_{FS} - c_0)$ where $c_{FS} = 5.2517\text{ \AA}$ is the out-of-plane lattice parameter of GaN fully strained on AlN.

Regarding the FWHM of the ω -scans around the (0002) reflections of the different layers ($\Delta\omega$ values in Table I), the increase of $\Delta\omega_{GaN}$ and $\Delta\omega_{SL}$ in the etched samples in comparison with the as-grown structures is explained, on the one hand, by the nanostructuration, and, on the other hand, by the expected strain relaxation towards the pillar side walls. The $\omega - 2\theta$ reflections assigned to the superlattice do not present any significant angular shift before and after etching. However, the intensity of the peaks related to the superlattice and to the GaN buffer layer decreases to about 10% of the as-grown value, if we take the intensity of the AlN substrate as a reference. This decrease is explained by the fact that there is only 10% of the material remaining after the etching process. In contrast, the reflection associated to GaN exhibits a clear, systematic shift towards larger angles in the etched structures, which is an indication of strain relaxation. The lattice parameter c_{GaN} extracted from these data and the strain along the growth axis, ϵ_{zz} , are listed in Table I. Full relaxation (within the error bar of the measure-

ments of $\pm 4\%$) of the GaN buffer is obtained for pillars with a diameter $\leq 0.4\text{ }\mu\text{m}$. Previous studies on GaN nanopillars have seen full relaxation only at the point where the pillar length (here GaN segment length) exceeds the pillar diameter [22].

The determination of the strain state of the superlattice requires information from asymmetric reflections. Therefore, reciprocal space maps around the $(\bar{2}025)$ reflection were collected for selected samples. Figures 2(b) and (c) show the reciprocal space maps for the sample NIR as-grown and etched to nanopillars with a diameter of $d = 0.1\text{ }\mu\text{m}$, respectively. In both cases, several satellites of the superlattice reflection can be identified, which appear at an intermediate Q_x vector between the AlN substrate and the GaN buffer layer. The Q_x location of the reflections related to the superlattice does not vary with etching; it is only the reflection from the GaN buffer layer that exhibits a drastic shift, consistent with the observations in the $\omega - 2\theta$ scans. This behavior indicates that the strain state of the superlattice is decoupled from the strain state of the underlying GaN layer. Extracting the average lattice parameter c of the superlattice from the $\omega - 2\theta$ diffractogram and its average in-plane lattice parameter from the reciprocal space map, we estimate an average Al concentration in the structure of $65 \pm 1\%$, and that the superlattice is fully relaxed. This result explains the insensitivity of the superlattice to the strain state of the GaN underlayer and is in agreement with Kandaswamy *et al.* [23], who have shown that full relaxation of similar GaN/AlN superlattices can be achieved after the growth of about 10 GaN/AlN periods independently of the substrate. The simulations of the $\omega - 2\theta$ scans in Figure 2(a) take into account the composition and strain states extracted from the reciprocal space maps.

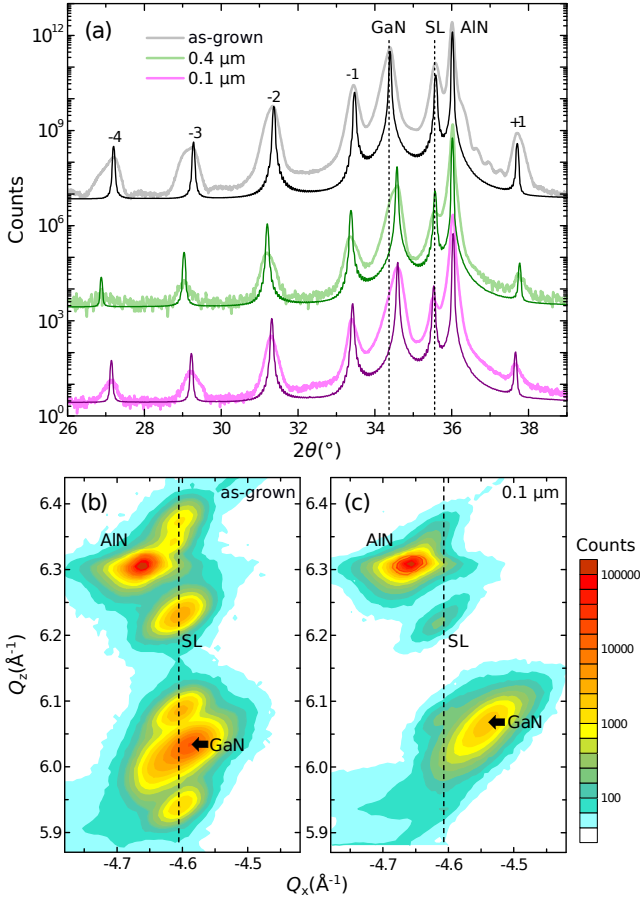


FIG. 2. (a) XRD $\omega - 2\theta$ scans around the (0002) reflection of sample NIR as-grown and etched into pillars with $d = 0.4$ and $0.1 \mu\text{m}$. Superimposed are the simulated profiles. Additionally, reciprocal space maps around the (2025) reflection are shown for sample NIR (b) as-grown and (c) etched into nanopillars with $d = 0.1 \mu\text{m}$.

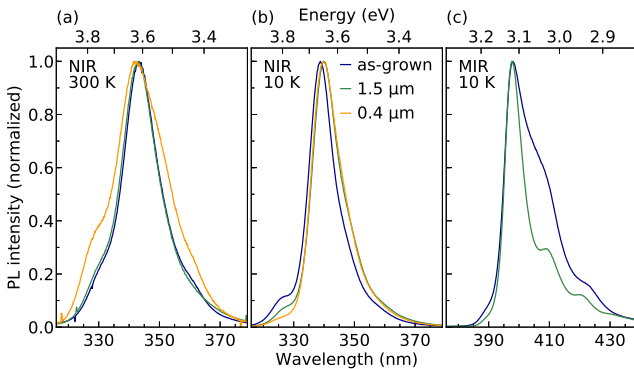


FIG. 3. (a) Room-temperature and (b) low-temperature PL spectra for sample NIR in the as-grown state, as well as for pillar diameters of 1.5 and $0.4 \mu\text{m}$. (c) Low-temperature PL spectra for sample MIR as-grown and etched into $1.5 \mu\text{m}$ pillars.

B. Interband emission

To get a first idea about the impact of the top-down processing on the optical characteristics, we have studied the PL emission of the heterostructures. Exemplary spectra from sample NIR recorded at room temperature (300 K), and from both samples NIR and MIR at low temperature (10 K) are presented in Figs. 3(a)–(c). For sample NIR, the emission is centered around 343 nm at room temperature and around 339 nm at 10 K. In comparison, $\mathbf{k}\cdot\mathbf{p}$ calculations predict interband transition wavelengths of 342 nm at 300 K and 335 nm at 10 K, which confirms the validity of these simulations (note that excitonic effects are not taken into account). For sample MIR, the low-temperature PL emission wavelength of 400 nm also coincides with the calculated interband transition energy. However, for this sample, the PL signal could not be detected at 300 K, a consequence of the strong quantum confined Stark effect in these wide QWs. Note that both samples do not exhibit any significant shift of the PL emission wavelength after etching. This behavior is in agreement with the XRD results for the superlattice, which is relaxed already after growth and shows no variation of the strain state after etching.

The measured low temperature PL intensities, normalized to the emission of the as-grown samples, and the ratios between the integrated intensities I_{PL} at 300 and 10 K (only for sample NIR) are summarized in Table I. Strikingly, the emission intensity at 10 K is not significantly degraded by the etching, the attenuation amounts to less than a factor of 2. Considering that the top-down processing removes about 80% of the material in the case of the micropillars (pitch = $2 \times$ diameter) and 90% of the material in the case of the nanopillars (pitch = $3 \times$ diameter), this result indicates that the in- and outcoupling of the ultraviolet light is significantly improved for the pillar arrays as compared to the planar layers [24, 25]. At the same time, compared with the as-grown planar reference, the ratio $I_{\text{PL}}(300 \text{ K})/I_{\text{PL}}(10 \text{ K})$ shows a trend to smaller values with decreasing feature size, with the reduction being limited to a factor of 3 in the case of the $0.2 \mu\text{m}$ sample. Apparently, the processing induces some nonradiative defects at or close to the surface, which are activated at room temperature. However, it is a notable result – also important for intersubband device applications – that, even for the smallest pillar diameter, the non-radiative recombination is only moderately enhanced. Note that no additional processing [26] for defect removal or surface passivation has been applied after the ICP etching process.

C. Intersubband absorption

Turning to the intersubband absorption, room-temperature FTIR transmittance spectra for the samples prior to (as-grown) and after the top-down processing are given in Fig. 4. For the as-grown samples, a clear absorption dip appears at $\lambda = 1.5 \mu\text{m}$ (0.83 eV) for the sample NIR and at $\lambda = 4.4 \mu\text{m}$ (0.28 eV) for the sample MIR. These

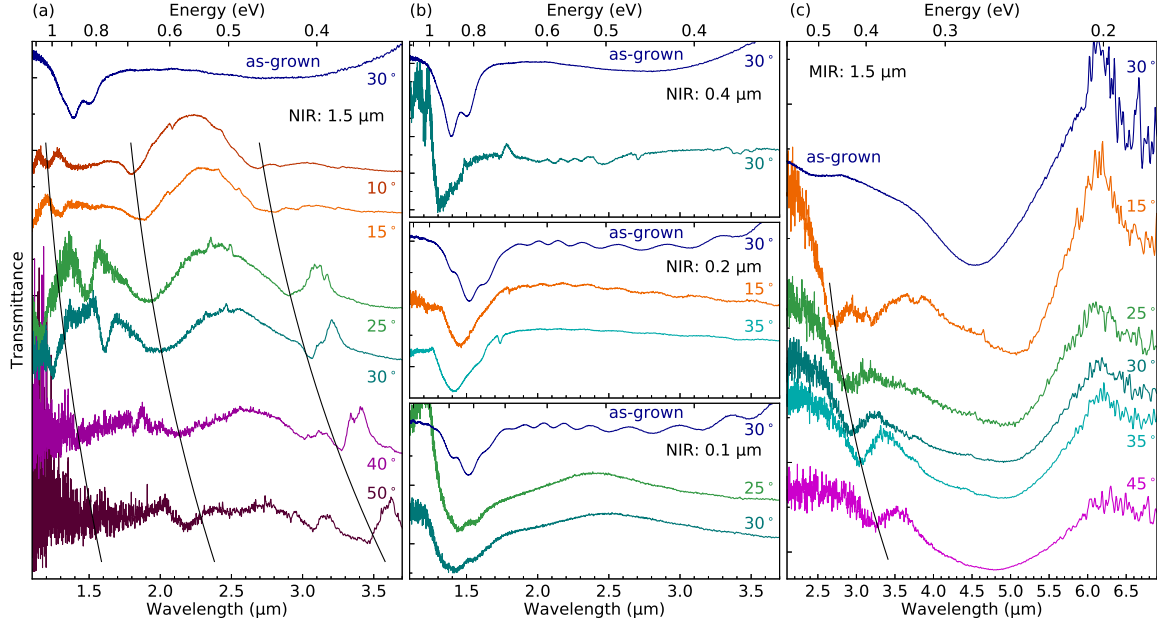


FIG. 4. FTIR transmittance of the as-grown compared with the top-down-processed samples for (a), (b) the sample NIR and (c) the sample MIR. The diameter of the pillars is 1.5 μm in (a), (c), while it is 0.4, 0.2, and 0.1 μm (top to bottom) for the different panels in (b). The incident angle θ_{in} is indicated for each curve. The black lines in (a) and (c) are guides to the eye highlighting absorption features related to the photonic crystal that shift with the measurement angle.

energies are in good agreement with the $\mathbf{k}\cdot\mathbf{p}$ calculations given above.

For the sample NIR etched down to micropillars ($d = 1.5 \mu\text{m}$), Fig. 4(a) displays the infrared transmittance measured at different angles compared to a measurement of the same sample piece recorded before etching. After etching, the spectra exhibit several absorption related dips in intensity, which shift with the measurement angle, as indicated by the black lines serving as a guide to the eye. These features in the spectra can be attributed to the fact that the micropillar array constitutes a two-dimensional photonic crystal with a lattice constant a_p on the order of the investigated wavelength range [17]. The lattice constant of the photonic crystal viewed by the light depends on the angle of incidence of the light on the pillars θ_s , which in turn depends on the angle of incidence of the light on the sample facet θ_{in} and the refractive indices of the substrate and the active region. The result is a dependence of the wavelength of the photonic crystal related absorption on the measurement angle. In contrast, a shift in wavelength would not be expected for intersubband absorption. A full electrodynamics-based modeling necessary to understand these photonic crystal features in detail is beyond the scope of the current manuscript.

If we want to avoid photonic crystal resonances overlapping with the intersubband absorption, the pillar size must be decreased to diameters far enough below the intersubband absorption wavelength. Following this approach, normalized infrared transmittance spectra for sample NIR with sub-wavelength nanopillar diameters of $d = 0.4 \mu\text{m}$, $d = 0.2 \mu\text{m}$, and $d = 0.1 \mu\text{m}$ are shown in Fig. 4(b) (top to bottom). In all three samples, the dip related to the intersubband absorp-

tion, located around 1.5 μm , is clearly visible both before and after the etching of the nanopillars. Spectra recorded at different angles show that this feature does not shift, which confirms that it originates from the intersubband transition. The magnitude of the absorption dip at an angle of 30–35° is $67 \pm 8\%$ in the as-grown samples and $72 \pm 12\%$ in the samples etched into nanopillars, which means that there is no degradation of the total ISB absorption in spite of the fact that 90% of the material was etched away. Table I also shows the FWHM of the absorption before and after etching. This value is essentially unchanged except for the smallest pillar diameter ($d = 0.1 \mu\text{m}$). As with the PL intensity, we do not have a significant degradation of the intersubband absorption characteristics, even though all the measurements are performed at room temperature. However, we note that the center of the absorption feature is slightly blueshifted for the nanopillars as summarized in Table I. The blueshift amounts to 0.04–0.12 μm (20–70 meV higher energy) without apparent trend with the pillar diameter. This shift cannot be associated to misfit relaxation, since XRD data show no variation in the strain state of the superlattice. The shift is not related either to carrier trapping, since a decrease in the density of carriers available for absorption would shift the emission towards longer wavelengths [27].

In the case of sample MIR patterned into 1.5 μm pillars, the absorption wavelength is shifted away from the photonic crystal resonances associated to the pillar array. Fig. 4(c) shows the IR transmittance of sample MIR measured before and after etching. After etching, the intersubband absorption band centered around $\lambda = 4.6 \mu\text{m}$ dominates the spectra, without significant shift as a function of the angle. The

central wavelength is redshifted (by 0.2 μm) compared with the measurement for the as-grown sample. Again, there is no variation of the magnitude of the absorption in spite of the reduction of the total absorbing material by 80%.

IV. CONCLUSIONS AND OUTLOOK

We presented a systematic analysis of intersubband absorption in group-III nitride micro- and nanopillars for different pillar diameters and absorption wavelengths in the near- and mid-IR. As a consequence of the top-down processing, a relaxation of the strain in the GaN buffer layer is observed in XRD measurements, while reciprocal space maps show that the GaN/AlN superlattice is fully relaxed already for the as-grown samples. In line with XRD results, the PL emission of the superlattice does not show any spectral shift for the processed samples. At the same time, the improved in- and outcoupling of light for the pillar arrays compensates for the etching away of a large part of the emitting material as seen from the PL intensities at 10 K. Only at room temperature, the non-radiative recombination at the pillar sidewalls has a moderate effect on the PL intensity.

Concerning the infrared absorption, we showed that when the spacing of the pillar array is comparable to the wave-

length of the investigated spectral region, photonic crystal resonances dominate the IR absorption spectra. For sub-wavelength pillar arrays, where these resonances are at much shorter wavelengths than the intersubband absorption, the absorption is clearly evidenced. We have shown that the magnitude and linewidth of the intersubband absorption is preserved in spite of the low filling factor even when 80% or 90% of the material is etched away. This result is in contrast to studies of micropillar quantum cascade lasers, where a high fill factor is required to achieve sufficient gain [15]. In summary, this work is opening the pathway for a microstructured group-III nitride quantum-well infrared photodetector and can be seen as a motivation to pursue the investigation of group-III nitride pillars also for intersubband emitter structures.

ACKNOWLEDGMENTS

Sample processing has been carried out in the Nanofab cleanroom of CNRS Institut Néel and the PTA cleanroom of CEA-Grenoble. The authors would like to thank Bruno Fernandez at Nanofab for technical support with the laser lithography, as well as Luca Redaelli and Yoann Curé for their assistance with calculations. Financial support from the EU ERC-SG “TeraGaN” (#278428) is acknowledged.

-
- [1] C. B. Lim, A. Ajay, J. Lähnemann, D. A. Browne, and E. Monroy, in *Handbook of GaN Semiconductor Materials and Devices*, Series in Optics and Optoelectronics, edited by Wengang (Wayne) Bi, Haochung (Henry) Kuo, Peicheng Ku, Bo Shen (CRC Press (Taylor & Francis Group), 2017) pp. 615–644.
 - [2] N. Binggeli, P. Ferrara, and A. Baldereschi, *Phys. Rev. B* **63**, 245306 (2001).
 - [3] M. Tchernycheva, L. Nevou, L. Doyennette, F. Julien, E. Warde, F. Guillot, E. Monroy, E. Bellet-Amalric, T. Remmele, and M. Albrecht, *Phys. Rev. B* **73**, 125347 (2006).
 - [4] C. Edmunds, L. Tang, M. Cervantes, M. Shirazi-HD, J. Shao, A. Grier, A. Valavanis, J. D. Cooper, D. Li, G. Gardner, D. N. Zakharov, Z. Ikonić, D. Indjin, P. Harrison, M. J. Manfra, and O. Malis, *Phys. Rev. B* **88**, 235306 (2013).
 - [5] N. Iizuka, K. Kaneko, N. Suzuki, T. Asano, S. Noda, and O. Wada, *Appl. Phys. Lett.* **77**, 648 (2000).
 - [6] C. Gmachl, S. Frolov, H. Ng, S.-N. Chu, and A. Cho, *Electron. Lett.* **37**, 378 (2001).
 - [7] E. Bellotti, K. Driscoll, T. D. Moustakas, and R. Paiella, *Appl. Phys. Lett.* **92**, 101112 (2008).
 - [8] C. Edmunds, J. Shao, M. Shirazi-HD, M. J. Manfra, and O. Malis, *Appl. Phys. Lett.* **105**, 021109 (2014).
 - [9] M. Beeler, P. Hille, J. Schörmann, J. Teubert, M. de la Mata, J. Arbiol, M. Eickhoff, and E. Monroy, *Nano Lett.* **14**, 1665 (2014).
 - [10] J. Lähnemann, A. Ajay, M. I. Den Hertog, and E. Monroy, *Nano Lett.* **17**, 6954 (2017).
 - [11] J. Lähnemann, M. Den Hertog, P. Hille, M. de la Mata, T. Fournier, J. Schörmann, J. Arbiol, M. Eickhoff, and E. Monroy, *Nano Lett.* **16**, 3260 (2016).
 - [12] A. Ajay, C. B. Lim, D. A. Browne, J. Polaczyński, E. Bellet-Amalric, J. Bleuse, M. I. den Hertog, and E. Monroy, *Nanotechnology* **28**, 405204 (2017).
 - [13] P. K. Kandaswamy, F. Guillot, E. Bellet-Amalric, E. Monroy, L. Nevou, M. Tchernycheva, A. Michon, F. H. Julien, E. Baumann, F. R. Giorgetta, D. Hofstetter, T. Remmele, M. Albrecht, S. Birner, and L. S. Dang, *J. Appl. Phys.* **104**, 093501 (2008).
 - [14] A. Vardi, G. Bahir, S. E. Schacham, P. K. Kandaswamy, and E. Monroy, *Phys. Rev. B* **80**, 155439 (2009).
 - [15] M. I. Amanti, A. Bismuto, M. Beck, L. Isa, K. Kumar, E. Reimhult, and J. Faist, *Opt. Express* **21**, 10917 (2013).
 - [16] M. Krall, M. Brandstetter, C. Deutsch, H. Detz, A. M. Andrews, W. Schrenk, G. Strasser, and K. Unterrainer, *Opt. Express* **22**, 274 (2014).
 - [17] M. Krall, M. Brandstetter, C. Deutsch, H. Detz, A. M. Andrews, W. Schrenk, G. Strasser, and K. Unterrainer, *IEEE J. Sel. Top. Quantum Electron.* **21**, 780 (2015).
 - [18] M. Karimi, M. Heurlin, S. Limpert, V. Jain, X. Zeng, I. Geijselaers, A. Nowzari, Y. Fu, L. Samuelson, H. Linke, M. T. Borgström, and H. Pettersson, *Nano Lett.* **18**, 365 (2018).
 - [19] E. Bellet-Amalric, C. Adelman, E. Sarigiannidou, J. L. Rouvière, G. Feuillet, E. Monroy, and B. Daudin, *J. Appl. Phys.* **95**, 1127 (2004).
 - [20] S. Birner, T. Zibold, T. Andlauer, T. Kubis, M. Sabathil, A. Trellakis, and P. Vogl, *IEEE Trans. Electron Devices* **54**, 2137 (2007).
 - [21] S. Albert, A. Bengoechea-Encabo, M. Sabido-Siller, M. Müller, G. Schmidt, S. Metzner, P. Veit, F. Bertram, M. Sánchez-García, J. Christen, and E. Calleja, *J. Cryst. Growth* **392**, 5 (2014).

- [22] M. Hugues, P. A. Shields, F. Sacconi, M. Mexis, M. Auf der Maur, M. Cooke, M. Dineen, A. Di Carlo, D. W. E. Allsopp, and J. Zúñiga-Pérez, *J. Appl. Phys.* **114**, 084307 (2013).
- [23] P. K. Kandaswamy, C. Bougerol, D. Jalabert, P. Ruterana, and E. Monroy, *J. Appl. Phys.* **106**, 013526 (2009).
- [24] N. P. Reddy, S. Naureen, S. Mokkapati, K. Vora, N. Shahid, F. Karouta, H. H. Tan, and C. Jagadish, *Nanotechnology* **27**, 065304 (2016).
- [25] C. Hauswald, I. Giunttoni, T. Flissikowski, T. Gotschke, R. Calarco, H. T. Grahn, L. Geelhaar, and O. Brandt, *ACS Photonics* **4**, 52 (2017).
- [26] C. Li, S. Liu, T. S. Luk, J. J. Figiel, I. Brener, S. R. J. Brueck, and G. T. Wang, *Nanoscale* **8**, 5682 (2016).
- [27] A. Helman, M. Tchernycheva, A. Lussan, E. Warde, F. H. Julien, K. Moumanis, G. Fishman, E. Monroy, B. Daudin, D. Le Si Dang, E. Bellet-Amalric, and D. Jalabert, *Appl. Phys. Lett.* **83**, 5196 (2003).